TURBULENCE INTENSITY EFFECT ON SUB-CRITICAL VIBRATION FOR AN ELASTIC CYLINDER SUBJECT TO AXIAL FLOW

Chu S.X.* and Li B.
*Author for correspondence
Institute for Turbulence-Noise-Vibration Interaction and Control,
Shenzhen Graduate School, Harbin Institute of Technology,
Shenzhen, 518055,
China,
E-mail: s_x_chu@163.com

ABSTRACT

Effect of inlet turbulence intensity on sub-critical vibration is numerical studied for an elastic cylinder subject to axial tubular fluid flow. The cylinder is fixed at both ends and is free to vibrate in any transverse directions. The ANSYS mechanical APDL+FLUENT two-way system coupling is adopted to simulate the fluid-structure interaction. The large eddy simulation model and dynamic model are applied to the modeling of the turbulent flow and re-meshing, respectively. The stiffness and flow velocity are combined into the formulae of the dimensionless flow velocity. The sub-critical vibration of the single cylinder for different inlet turbulence intensity (0%~15%) at the sub-critical velocity (3.3) is studied. The results show that the amplitude of the sub-critical vibration increases by increasing inlet turbulence intensity. With the increase of inlet turbulence intensity, the random vibration occurs. The increasing inlet turbulence intensity is the primary cause of the random vibration. However, there is no buckling for higher inlet turbulence intensity at the sub-critical velocity. With the increasing inlet turbulence intensity, the vibration mode exhibits the first vacuum beam mode at the first, and then the high order mode (e.g., the second mode), and again the first vacuum beam mode at the last.

INTRODUCTION

The axial-flow-induced vibration, especially the small amplitude vibration produced by the flow velocity below the so-called critical velocities for buckling or flutter, has been given a great deal of attention in the literature, due to its important applications such as in nuclear reactors. See Païdoussis [1] for an excellent compendium of this topic. It has been experimentally found that the structural response is sensitive to the flow entrance conditions [2, 3]. Furthermore, the incident flow of the clustered fuel rods is always turbulent in practice. However, the information in the literature on how the inlet turbulence intensity affects the fluid-structure interaction is very limited [4]. This motivates the present work to investigate numerically how an elastic cylinder subjected to an axial tubular flow responds to the varying incident turbulent intensity. The numerical calculation is compared with experimental data obtained in a water tunnel.

PHYSICAL MODEL AND NUMERICAL SIMULATION

Figure 1 presents schematically a single elastic cylinder subjected to an axial tubular flow. The cylinder of D in diameter is clamped at two ends, where the displacement and angle of rotation are all zero in the x, y and z directions. The length L between the clamped points is $20D$. Assuming an infinitely long cylinder, there is no flow separation at the clamped points. The axial flow is confined by a cylindrical wall of the same length as the cylinder and $12D$ in diameter. The origin of the coordinate system is defined at mid-point on the cylinder axis between the clamped points. The incident flow is uniform at the inlet, i.e., the upstream clamped point. The cylinder is free to vibrate in both x and y directions. The dimensionless flow velocity is defined by $\bar{U} = v_0 L\sqrt{\rho A_t / EI}$, where v_0, ρ, A_t, and EI are the mean axial flow velocity at the inlet, fluid density, cross-sectional area of the cylinder, and modulus of flexural rigidity, respectively. The flow pressures at the inlet and outlet are

$$p_t\big|_{z=-10D} = \rho v_0^2/2, \ p\big|_{z=10D} = 0 \qquad (1)$$

respectively.

The fluid and structural motions are governed by the mass conservation and Navier-Stokes equations along with the transient structural dynamics equation, viz.

$$\nabla \cdot \vec{v} = 0 \qquad (2)$$

$$\rho \frac{\partial \vec{v}}{\partial t} + \rho\left(\vec{v} - \vec{\hat{v}}\right) \cdot \nabla \vec{v} = -\nabla p + \mu \nabla^2 \vec{v} \qquad (3)$$

$$\mathbf{M}\vec{\ddot{u}} + \mathbf{C}\vec{\dot{u}} + \mathbf{K}\vec{u} = \vec{F}(t) \qquad (4)$$

where t, $\vec{v}$, and μ are time , fluid velocity vector, and dynamic viscosity, respectively. The $\vec{\hat{v}}$ is the velocity vector of the moving mesh, and $\mathbf{M}$, $\mathbf{C}$, $\mathbf{K}$, $\vec{\ddot{u}}$, $\vec{\dot{u}}$, $\vec{u}$ and $\vec{F}(t)$ are mass matrix, damping matrix ,stiffness matrix, nodal acceleration vector, nodal velocity vector, nodal displacement vector and load vector, respectively. The above equations are iteratively solved numerically by ANSYS mechanical

APDL+FLUENT two-way coupling [5]. Firstly, ANSYS Fluent transfers the pressure force on the cylinder to ANSYS Mechanical. Secondly, ANSYS Mechanical calculates the structural deformation, and transmits this to Fluent. Then, Fluent modifies the mesh to resolve the mesh motion. Within one time step, the mesh in the fluid domain is updated by dynamic mesh with the diffusion and re-meshing method. Large eddy simulation (LES) model is used presently and the sub-grid scale (SGS) is modeled by Smagorinsky-Lilly model, where Smagorinsky constant C_s is 0.1. The second-order implicit method is adopted for time discretization as LES model requires second-order solution in ANSYS Fluent software.
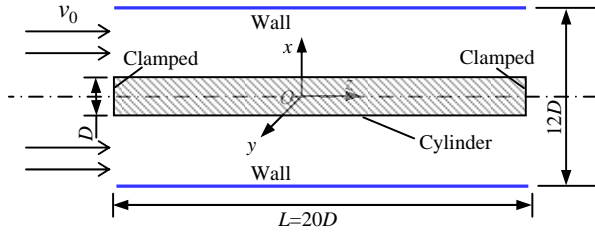

Figure 1 Schematic of physical model

The mesh is created by ANSYS Meshing. To ensure the mesh quality, the fluid domain is divided into two sub-regions, i.e., the boundary layer and the main flow, where the elements are hexahedron and prism, respectively. The dynamic mesh is applied in the boundary layer. Grid-refinement studies are performed to ensure that the calculated results are independent of the grid size. The number of element in fluid domain is about 68 8600, and the cross-sectional mesh is shown in Figure 2.

Figure 2 Mesh of mid-cross-section

RESULTS AND DISCUSSIONS

The dimensionless x- and y-displacements and axial coordinate and time are defined by

$$X^* = u_x/D, Y^* = u_y/D, z^* = (z+L/2)/D \qquad (5)$$

$$\tau = t\sqrt{EI/(\rho_b A_e + \rho A_t)}/L^2 \qquad (6)$$

where ρ_b and A_e are the density of the solid cylinder and effective area, respectively. The displacements are analyzed by FFT and the dimensionless frequency is defined by

$$\bar{f} = fL^2\sqrt{\rho_b A_e + \rho A_t/EI} \qquad (7)$$

where f is frequency. Eqs (2)-(4) are solved for $T_u = 0\%$, 0.01%, 0.02%, 0.03%, 0.3%, 2%, 5%, 7% and 10%,

respectively. In each case, the cylinder is initially at its equilibrium state, that is, there is no pre-displacement.

The computational code had been verified by comparing the experiment measurements with numerical simulation results [6]. The comparison results show that the root mean square values, X^*_{rms} and Y^*_{rms}, of X^* and Y^* at $z^* = 10$ agree well between calculation and measurement over $\bar{U} = 0.075 - 1.9179$ for the same T_u (=0.3%).

As shown in Figre 3, T_u has a significant effect on X^* and Y^* ($\bar{U} = 3.3$) at $z^* = 10$, which are quite small at $T_u = 0.01\%$, with their maximum in the order of 10^{-3}. However, both X^* and Y^* grow greatly with the increasing T_u, their maximum amplitudes reaching 0.024 and 0.03, 0.025and 0.05 for $T_u = 5\%$ and 7%, respectively.
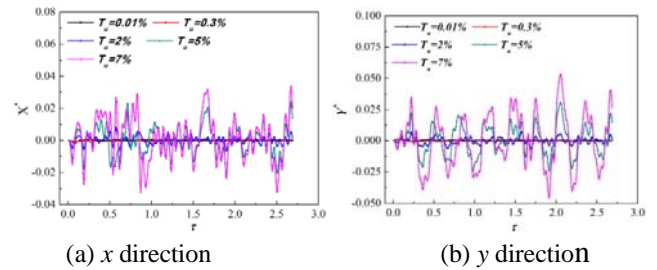
(a) x direction　　　　(b) y direction

Figure 3 Variation of dimensionless displacements at mid-span ($z^* = 10$) with dimensionless time under different inlet turbulence intensity at $\bar{U} = 3.3$

The RMS values, X^*_{rms} and Y^*_{rms} of X^* and Y^* at mid-span ($z^* = 10$) under different inlet turbulence intensity at $\bar{U} = 3.3$ are given in Figure 4(a) and (b), respectively. With the increasing T_u, the RMS values, both X^*_{rms} and Y^*_{rms} of X^* and Y^* at mid-span ($z^* = 10$) increase.
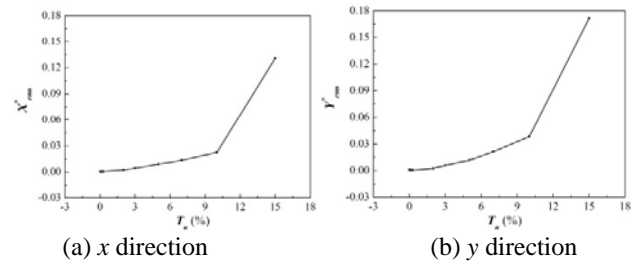
(a) x direction　　　　(b) y direction

Figure 4 RMS values, X^*_{rms} and Y^*_{rms} of X^* and Y^* at mid-span ($z^* = 10$) under different inlet turbulence intensity at $\bar{U} = 3.3$

As stated above, the amplitude of X^* and Y^* increases with the increasing T_u. However, with the increase of T_u, no buckling occurs at sub-critical velocity. Figure 5 shows the f X^* and Y^* at mid-span ($z^* = 10$) varies with time when $\bar{U} = 3.3, T_u = 10\%$. The random vibration occurs around zero-equilibrium state.

The trajectory plots for $\bar{U} = 3.3$ under different inlet turbulence intensity are sown in Figure 6. With the increasing T_u, the scope of black dots increase, which also indicates the

amplitudes of the cylinder increase. When the inlet turbulence intensity T_u increases to 10%, the trajectory exhibits the random vibration around zero-equilibrium stat. The zero state is also the stationary point and no buckling occurs.
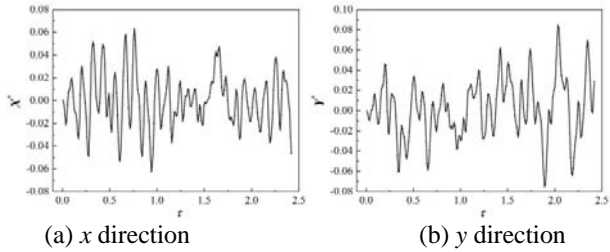

(a) x direction　　　　　(b) y direction

Figure 5 Variation of dimensionless displacements at mid-span (z* = 10) with dimensionless time at $\bar{U} = 3.3, T_u = 10\%$

(a) $T_u = 0.01\%$　　　　(b) $T_u = 0.3\%$

(c) $T_u = 2\%$　　　　(d) $T_u = 5\%$

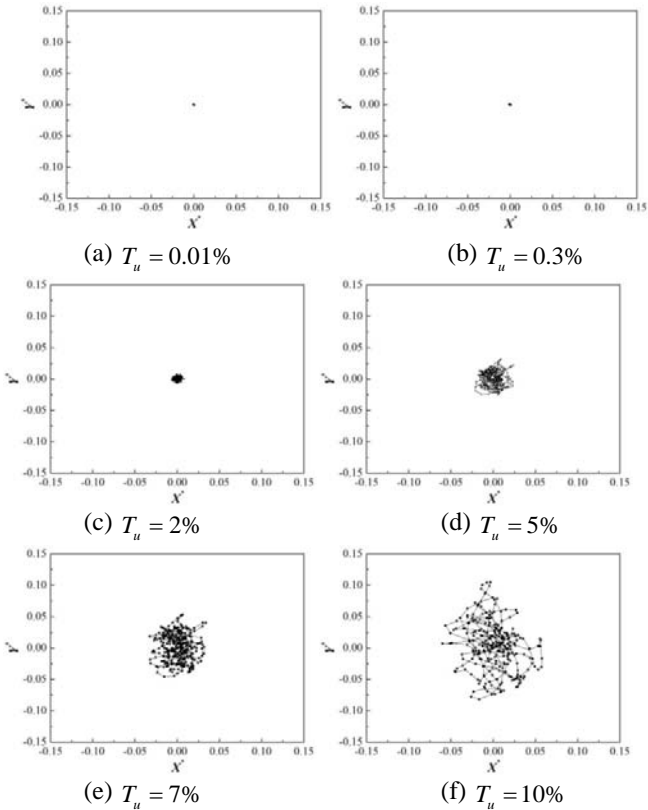(e) $T_u = 7\%$　　　　(f) $T_u = 10\%$

Figure 6 Trajectory of mid-span (z* = 10) cross-section under different inlet turbulence intensity at $\bar{U} = 3.3$

The RMS values, X^*_{rms} and Y^*_{rms} of X^* and Y^* along the axial direction at $\bar{U} = 3.3, T_u = 0.2\%, 2\%, 5\%, 10\%$ are given in Figure 7(a), (b), (c) and (d) respectively. The RMS values, X^*_{rms} and Y^*_{rms} show the symmetric parabolic pattern in which the maximums occurs at mid-span (z* = 10), which indicates that the dominant beam shape is the first vacuum beam mode both in x- and y- direction. However, at $T_u = 2\%$, X^*_{rms} and Y^*_{rms} exhibits an axial M-shaped distribution. Furthermore, at $T_u = 5\%$, only X^*_{rms} exhibits axial M-shaped distribution, and both X^*_{rms} and Y^*_{rms} gradually tends to the first vacuum beam

mode. At $T_u = 15\%$, it can be clearly seen from Figure 7(d) that the dominant beam shape in x-direction is totally the first vacuum beam mode.
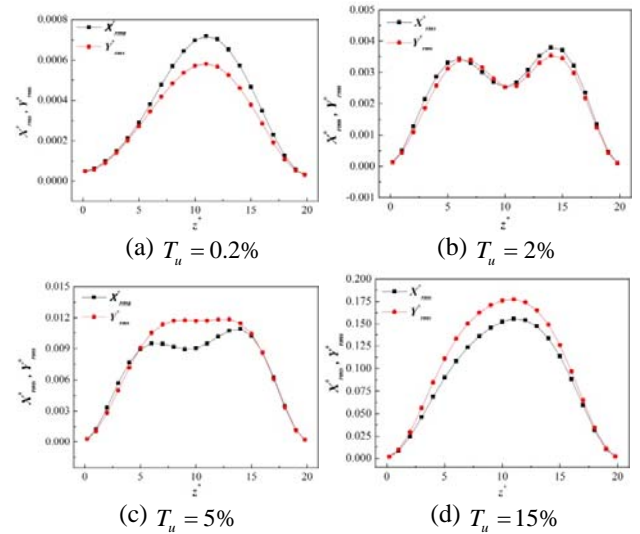

(a) $T_u = 0.2\%$　　　　(b) $T_u = 2\%$

(c) $T_u = 5\%$　　　　(d) $T_u = 15\%$

Figure 7 RMS values, X^*_{rms} and Y^*_{rms} of X^* and Y^* under different inlet turbulence intensity at $\bar{U} = 3.3$

(a) $T_u = 0\%$　　　　(b) $T_u = 0.3\%$

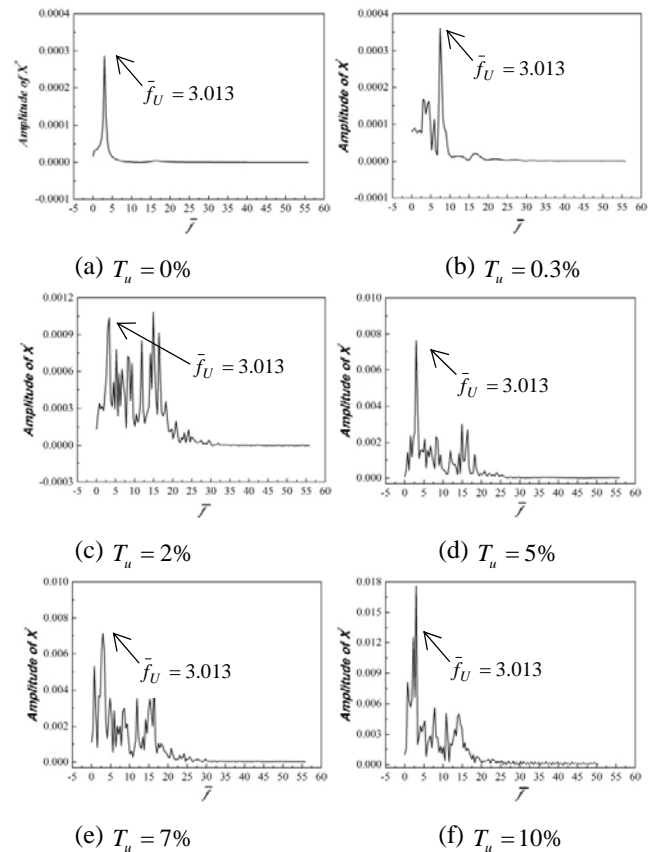(c) $T_u = 2\%$　　　　(d) $T_u = 5\%$

(e) $T_u = 7\%$　　　　(f) $T_u = 10\%$

Figure 8 Amplitude of x-displacement mid-span (z* = 10) cross-section under different inlet turbulence intensity at $\bar{U} = 3.3$

Figure 8 and Figure 9 show the amplitude of the displacements signals at mid-span (z* = 10) in x- and y-direction under different inlet turbulence intensity at $\bar{U} = 3.3$, respectively. The dimensionless dominant frequency $\bar{f}_{\bar{U}}$ and $\bar{f}_{(\bar{U},T_u)}$, which are determined by the dimensionless velocity $\bar{U}$ only, and both dimensionless velocity $\bar{U}$ and inlet turbulence intensity T_u, respectively. At sub-critical dimensionless velocity, the first dimensionless dominant frequency $\bar{f}_{\bar{U}}$ keeps constant, however, the corresponding amplitude increases with the increasing T_u.
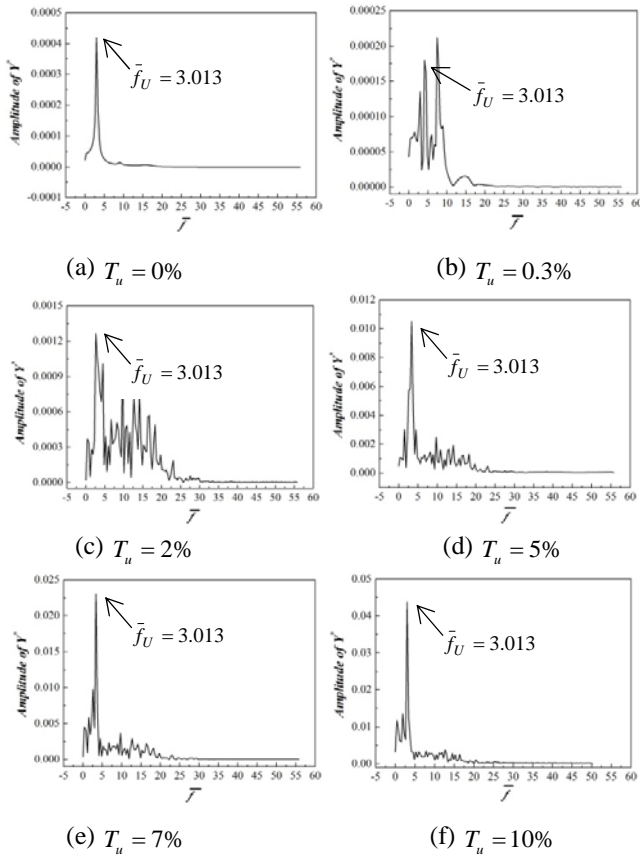

(a) $T_u = 0\%$ (b) $T_u = 0.3\%$

(c) $T_u = 2\%$ (d) $T_u = 5\%$

(e) $T_u = 7\%$ (f) $T_u = 10\%$

Figure 9 Amplitude of y-displacement mid-span (z* = 10) under different inlet turbulence intensity at $\bar{U} = 3.3$

At given inlet turbulence intensity, the amplitude corresponding to $\bar{f}_{(\bar{U},T_u)}$ is larger than that corresponding to $\bar{f}_{\bar{U}}$, as shown in Figure 8(c). The amplitude corresponding to $\bar{f}_{\bar{U}}$ is 0.00015, however, The amplitude corresponding to $\bar{f}_{(\bar{U},T_u)}$ is 0.0006. Hence, the dimensionless dominant frequency here is not $\bar{f}_{\bar{U}}$, but $\bar{f}_{(\bar{U},T_u)}$. The frequency corresponding to $\bar{f}_{(\bar{U},T_u)}$ is the second order frequency. Therefore, the X^*_{rms} and Y^*_{rms} exhibits an axial M-shaped distribution, which is shown in Figure 7(b).

With the further increasing T_u, the amplitude corresponding to $\bar{f}_{\bar{U}}$ is much larger than that corresponding to $\bar{f}_{(\bar{U},T_u)}$. The

dimensionless dominant frequency here is $\bar{f}_{\bar{U}}$, and the vibration mode is gradually tends to the first vacuum beam mode. The higher T_u, the more obvious trend. As shown in Figure 9(f), The amplitude in y-direction corresponding to $\bar{f}_{\bar{U}}$ is 0.045, and that corresponding to $\bar{f}_{(\bar{U},T_u)}$ is nearly 0.01. The vibration mode of the cylinder is the first vacuum beam mode again.

CONCLUSION

The effect of the inlet turbulent intensity on the axial-flow-induced vibration of an elastic cylinder is investigated numerically. The results show that the vibration amplitude grows with the increasing T_u, and there is no buckling for higher inlet turbulence intensity at the sub-critical velocity. The increasing T_u is the primary cause of the random vibration. The vibration mode exhibits the first vacuum beam mode at the first, and then the high order mode (e.g., the second mode), and again the first vacuum beam mode at the last.

ACKNOWLEDGEMENTS

REFERENCES

[1] Païdoussis M. P., Fluid-Structure Interactions: Slender Structures and Axial Flow, Vol. 2, 2004, Academic Press, Netherlands
[2] Swinson W F., Battiste R L., Luttrell C R. and Yahr G T., Follow-up fuel plate stability experiments and analyses for the advanced neutron source. United States Department of Energy. Oak Ridge National Laboratory, Oak Ridge Tennessee, 1993, pp 1-69
[3] Marcum W R. and Woods B G., Predicting the onset of dynamic instability of a cylindrical plate under axial flow conditions. Nuclear Engineering and Design, Vol. 250, 2012, pp. 81-100
[4] Wang L. and Ni Q., Vibration of slender structures subjected to axial flow or axially towed in quiescent fluid. *Advances in Acoustics and Vibration.* Article ID 432340, 19 pages, 2009, Hindawi Publishing Corporation
[5] ANSYS Inc., ANSYS 15.0 Documentation, 2014
[6] Chu S.X., Zhou Y., Li B., Turbulent intensity effect on the axial-flow-induced vibration of an elastic cylinder. 3rd Symposium on Fluid-Structure-Sound Interactions and Control, 05to 09 July, 2015, Perth, Western Australia